Check for updates

AGU100 ADVANCING EARTH AND SPACE SCIENCE

JGR Oceans

RESEARCH ARTICLE
10.1029/2019JC015232

Key Points:

- The European Space Agency's Envisat and CryoSat-2 satellites could provide continuous estimates of Arctic sea ice thickness dating back to 2002
- Envisat preferentially samples wider, thicker sea ice floes compared with CryoSat-2 and is more sensitive to reflection from off-nadir leads
- We reduce the positive Envisat sea ice thickness bias to negligible values, by accounting for its inability to sample discrete lead or floe surfaces

Correspondence to:
R. Tilling,
rachel.l.tilling@nasa.gov

Citation:
Tilling, R., Ridout, A., & Shepherd, A. (2019). Assessing the impact of lead and floe sampling on Arctic sea ice thickness estimates from Envisat and CryoSat-2. *Journal of Geophysical Research: Oceans*, *124*, 7473–7485. https://doi.org/10.1029/2019JC015232

Received 17 APR 2019
Accepted 23 SEP 2019
Published online 11 NOV 2019

Assessing the Impact of Lead and Floe Sampling on Arctic Sea Ice Thickness Estimates from Envisat and CryoSat-2

R. Tilling[1,2], **A. Ridout**[3], **and A. Shepherd**[4]

[1]Cryospheric Sciences Laboratory, NASA Goddard Space Flight Center, Greenbelt, MD, USA, [2]Earth System Science Interdisciplinary Center, University of MarylandCollege Park, MD, USA, [3]Centre for Polar Observation and Modelling, University College London, London, UK, [4]Centre for Polar Observation and Modelling, School of Earth and Environment, University of Leeds, Leeds, UK

Abstract Multidecadal observations of sea ice thickness, in addition to those available for extent, are key to understanding long-term variations and trends in the amount of Arctic sea ice. The European Space Agency's Envisat (2002–2010) and CryoSat-2 (2010–present) satellite radar altimeter missions provide a continuous 17-year dataset with the potential to estimate sea ice thickness. However, the satellite footprints are not equal in area and so different distributions of floes and leads are sampled by each mission. Here, we compare lead and floe sampling from Envisat and CryoSat-2 to investigate the impact of geometric sampling differences on Arctic sea ice thickness estimates. We find that Envisat preferentially samples wider, thicker sea ice floes, and that floes in less consolidated ice regions are effectively thickened by off-nadir ranging to leads. Consequently, Envisat sea ice thicknesses that are an average of 80 cm higher than CryoSat-2 over first-year ice and 23 cm higher over multiyear ice. By considering the along-track distances between lead and floe measurements, we are able to develop a sea ice thickness correction that is based on Envisat's inability to resolve discrete surfaces relative to CryoSat-2. This is a novel, physically based approach to addressing the bias between the satellites and reduces the average thickness difference to negligible values over first-year and multiyear ice. Finally, we evaluate our new bias-corrected Envisat sea ice thickness product using independent airborne, moored-buoy and submarine data. The European Space Agency's Envisat and CryoSat-2 satellites have the potential to produce a continuous record of Arctic sea ice thickness since 2002, but this is complicated by the fact that the satellites do not sample the sea ice surface in the same way. We find that Envisat is only able to sample larger, thicker sea ice relative to CryoSat-2, because of its poorer resolution. In this paper we account for these differences in sampling to combine Arctic sea ice thickness estimates from two the satellite missions. Applying a sea ice thickness bias correction to Envisat data reduces the ice thickness difference between Envisat and CryoSat-2 from an average of 53.0 to 0.5 cm

1. Introduction

The first estimates of sea ice thickness from satellite radar altimetry were produced using data from the European Space Agency's (ESA) European Remote Sensing (ERS) satellites, ERS-1 (1991–2000) and ERS-2 (1995–2011; Laxon et al., 2003). The ERS data revealed high-frequency inter-annual variability in winter sea ice thickness between 1993 and 2001, which was linked to changes in the length of the summer melt season. Following ERS, Giles et al. [2008] used ESA Envisat (2002–2012) data from 2002–2008 to show a thinning of winter sea ice across the Arctic after the 2007 record minimum September sea ice extent that year. Subsequent studies have used CryoSat-2 data to suggest that year-to-year fluctuations in winter Arctic sea ice thickness and volume since 2010 can be attributed to summer temperatures [Kwok & Cunningham, 2015; Tilling et al., 2015], wind-driven ice convergence [Kwok & Cunningham, 2015], and ice export through the Fram Strait [Ricker et al., 2018]. To quantify long-term trends in Arctic sea ice thickness and investigate the drivers of variability, it is necessary to combine multimission satellite data. Here we focus on combing sea ice thickness estimates from Envisat and CryoSat-2 using data from their common mission period of November 2010 to March 2012.

So far, only empirical solutions have been proposed to reconcile Arctic sea ice freeboard retrievals from Envisat with those from CryoSat-2. For example, Guerreiro et al. [2017] developed a radar freeboard

©2019. The Authors.
This is an open access article under the terms of the Creative Commons Attribution License, which permits use, distribution and reproduction in any medium, provided the original work is properly cited.

correction for Envisat data that is applied to the whole mission, based on the relationship between Envisat waveform shape and Envisat and CryoSat-2 freeboard difference over their common mission period. Another approach uses a consistent surface type classification scheme for both missions and an adaptive threshold retracker for Envisat sea ice waveforms to obtain the smallest difference in freeboard compared with CryoSat-2 [Paul et al., 2018]. However, no physically based solution for correcting the intermission sea ice freeboard and subsequent thickness bias currently exists. Differences in the satellite footprints will cause discrepancies in their discrimination of surface types. In this paper we investigate the impact of geometric sampling on sea ice thickness estimates from both missions and develop the first Envisat bias correction that is based on its sampling limitations. We also provide an uncertainty budget for our corrected Envisat sea ice thicknesses and evaluate the product using independent datasets.

2. Envisat and CryoSat-2—Operation and Data

The ESA Envisat satellite operated between March 2002 and April 2012 with a region of coverage (ROC) extending to 81.5° north and south [ESA, 2007]. Envisat's payload included the radar altimeter 2 (RA-2) instrument—a pulse-limited nadir-looking altimeter with primary Ku-band frequency of 13.575 GHz. A typical pulse-limited footprint for a Ku-band altimeter at an RA-2 altitude of 800 km [ESA, 2007] is estimated to be ~2 km [Chelton et al., 2001], assuming a surface with Gaussian height distribution. However, strong reflections from leads in the sea ice pack can dominate a radar echo from up to ~10 km off-nadir [Connor et al., 2009; Peacock & Laxon, 2004]. RA-2 samples are provided every 372 m along track. For this study we use the RA-2 instrument Sensor Data Record (SGDR), Level 2 (L2), version 2.1. The data are available from ESA at https://earth.esa.int/web/guest/-/ra-2-sensor-data-record-1471 and contain measurement information for averaged 18-Hz waveforms.

CryoSat-2 was launched by ESA in April 2010 and continues to observe the Polar Regions to within 2° of each pole [ESA/MSSL, 2013; Wingham et al., 2006]. Like the Envisat RA-2, the CryoSat-2 Synthetic Aperture Interferometric Radar Altimeter instrument operates in the Ku-band at a frequency of 13.575 GHz. Synthetic Aperture Interferometric Radar Altimeter is derived from a conventional pulse-limited altimeter instrument but utilizes synthetic aperture radar (SAR) processing to increase the CryoSat-2 resolution to approximately 300 m along track and 15 km across track, depending on satellite altitude [ESA/MSSL, 2013]. We use CryoSat-2 SAR and SAR interferometric mode Level 1b (L1b) data, available from ESA via an ftp client (ftp://science-pds.cryosat.esa.int). The Baseline-C L1b data contain measurement information for averaged 20-Hz waveforms. Both Envisat and CS-2 data include the echo power, satellite altitude, window delay, measurement time, geolocation, geophysical corrections, and numerous other instrument measurements.

3. Lead and Floe Sampling

3.1. Surface type Classification

We separate sea ice floe echoes from lead echoes by analyzing the waveform shape [Drinkwater, 1991; Laxon, 1994]. For both satellites, the pulse peakiness (PP) is calculated as the ratio of maximum to mean return power of the waveform, for bins where the return echo power is above the noise floor [Ridout, 2012; Tilling et al., 2018]. For CryoSat-2 we also account for the stack standard deviation (SSD) of each waveform, which is provided in the L1b product, and characterizes the spread of return power with incidence angle. Sea ice echoes from Envisat are defined as those with a PP less than 3 and from CyoSat-2 as those with a PP less than 9 and SSD greater than 4, for all waveforms with a sea ice concentration [Cavalieri et al., 1996, updated yearly above 75%. Lead echoes from Envisat have a PP greater than 30 and from CryoSat-2 a PP greater than 18 and SSD less than 4. We select different PP thresholds for Envisat and CryoSat-2 to account for the different echo characteristics of each instrument. Echoes that do not meet the classification criteria are considered ambiguous and removed from processing. Ambiguous echoes will occur if a mixture of leads and floes are present within the satellite footprint. Individual sea ice measurements are separated into first-year ice (FYI) and multiyear ice (MYI) ice using Norwegian Meteorological Service Ocean and Sea Ice Satellite Application Facility ice-type data [Andersen et al., 2012], which are available from October 2005.

To compare surface type discrimination from Envisat and CryoSat-2 we computed the percentage of echoes classified as floe, lead and ambiguous over their common mission period. The spatial distribution of lead

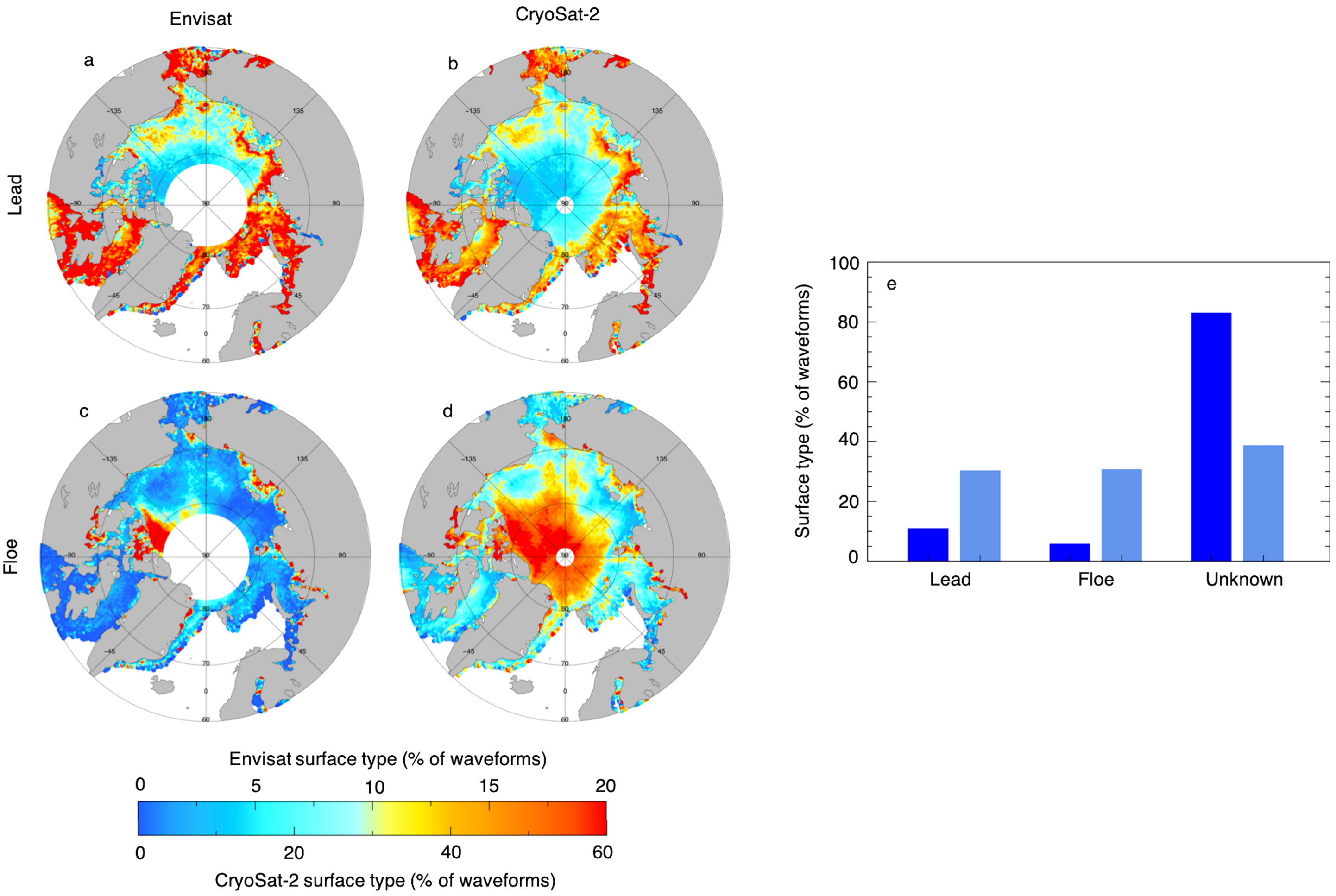

Figure 1. Surface type discrimination from Envisat and CryoSat-2 for the common mission period. Maps show the percentage of echoes defined as (a and b) lead or (c and d) floe for Envisat and CryoSat-2, respectively. Percentages were calculated on a 5 km^2 Polar Stereographic grid using all measurements within a 25 km radius of the center of each grid cell. (e) The percentage of individual echoes classified by Envisat (dark blue) and CryoSat-2 (light blue) as lead, floe, or unknown over the common mission region of coverage.

echoes is similar for Envisat (Figure 1a) and CryoSat-2 (Figure 1b). We observe the lowest percentage of leads north of Greenland and the Canadian Archipelago, and extending into the central Arctic [Tilling et al., 2018]—typically MYI regions associated with thick consolidated sea ice. Floe echoes show the opposite spatial distribution to leads for both Envisat (Figure 1c) and CryoSat-2 (Figure 1d), with fewer floe echoes over the southerly seasonal sea ice cover. Despite spatial similarities in their distribution, Envisat only discriminates 11% of echoes as lead and 6% as floe, compared with 30% for both surface types from CryoSat-2, over their common mission period and ROC (Figure 1e). The remaining 83% of Envisat waveforms are ambiguous compared with only 40% for CryoSat-2, as a consequence of its larger footprint encompassing a mixture of surface types. While CryoSat-2 discriminates an equal percentage of leads and floes, 5% more echoes are lead than floe from Envisat, suggesting that Envisat surface type mixing is more of a limitation for detecting diffuse floe returns than highly reflective lead returns, which can still dominate the signal from off-nadir [Armitage & Davidson, 2014]. Similar results have been found over Antarctic sea ice, where the fraction of lead waveforms to all waveforms is higher for Envisat than CryoSat-2 but with a comparable regional pattern [Schwegmann et al., 2016]. It is likely that the sensitivity of Envisat footprint geometry will limit its ability to resolve smaller sea ice floes in regions of mixed surface type or positively identify ice close to the floe edge.

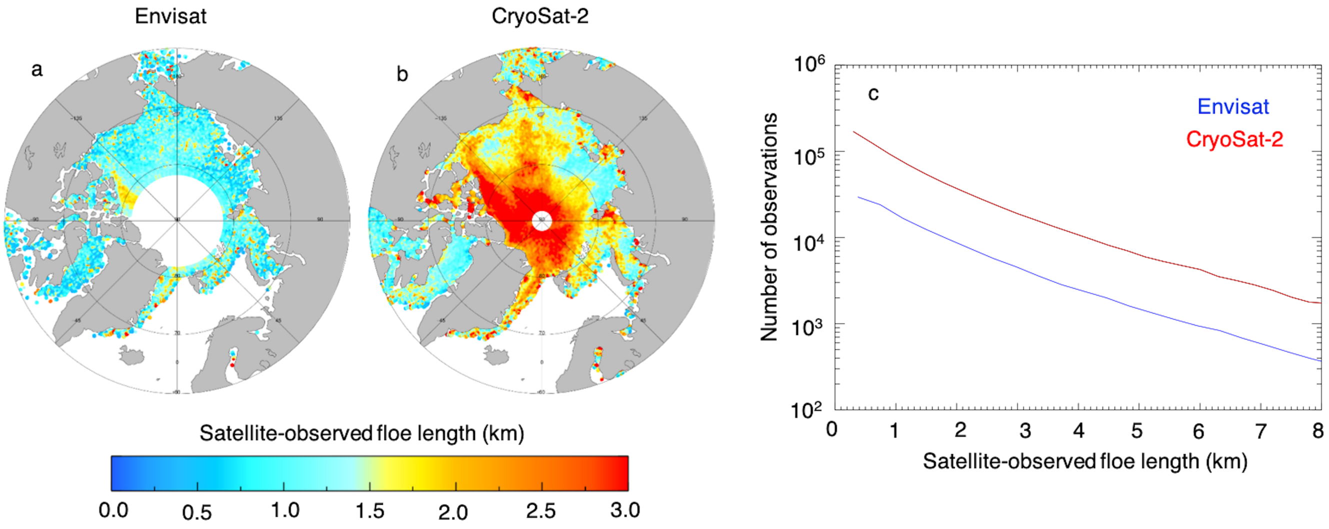

Figure 2. Satellite-observed floe lengths from Envisat and CryoSat-2 for the common mission period. Maps of satellite-observed floe length for (a) Envisat and (b) CryoSat-2 are produced on a 5 km^2 Polar Stereographic grid by averaging all measurements within a 25 km radius of the center of each grid cell, with each measurement receiving equal weighting. The maximum ice extent mask for the common mission period is shown in light gray. (c) Number of individual satellite-observed floe lengths in over the common mission region of coverage.

3.2. Satellite-Observed Floe Length

To investigate the limitations of Envisat in sampling the full sea ice floe size distribution, we calculate the floe lengths measured along track from Envisat and CryoSat-2. The satellite-observed floe length is the distance along track between the first and last measurement in a continuous sequence of echoes discriminated as floes. A gap of a one echo is permitted within the floe sequence to allow for anomalous ambiguous returns. These satellite-observed floe lengths are a proxy for true floe length as they are limited by the resolution of either satellite, and our method will underestimate floe length in cases where continuous floes are separated by the presence of more than one ambiguous return in sequence. However, the satellite-observed floe lengths measured by both satellites over their common mission period (Figures 2a and 2b) show a spatial pattern similar to the typical distribution of FYI and MYI across the Arctic [Tilling et al., 2018]. The satellite-observed floe length over FYI from Envisat is typically 1.6 km long and 1.9 km for CryoSat-2. Satellite-observed floe length increases over MYI to 2.3 km for Envisat and 3.0 km for CryoSat-2. Over their common mission period and ROC Envisat resolves approximately one sixth the number of satellite-observed floe length measurements as CryoSat-2 (Figure 2c). As both missions employ a similar sampling rate (section 2), the reduction in the number of measurements from Envisat must be a consequence of measurement dropout due to surface type mixing within its footprint (section 3.1). We believe Envisat sampling is limited to short sections of longer floes whereas CryoSat-2 is able to observe more of the floe length distribution, although it is not possible to infer this directly from our satellite measurements.

3.3. Distance Between Lead and Floe Measurements

Here we develop a metric to investigate the inability of Envisat to resolve discrete surfaces in sea ice covered regions. We calculate the lead-to-floe echo distance by measuring the distance between the last floe waveform in a sequence of floes and the first lead waveform encountered, and vice versa, for both Envisat and CryoSat-2. This is the distance over which mixed surfaces within the satellite footprint prevent surface type classification. Lead-to-floe echo distances from Envisat (Figure 3a) are consistently greater than those from CryoSat-2 (Figure 3b) over their common mission period, due to Envisat surface type mixing and measurement dropout. Over their common mission period and ROC, CryoSat-2 resolves floes to within a few hundred meters up to about 4.0 km of a lead, with an average lead-to-floe echo distance of 1.0 km. The travel distance required before resolving a discrete surface with Envisat data extends to an average of 11.3 km. Envisat also provides approximately one seventh the number of lead-to-floe echo distance measurements (Figure 3c). We conclude that the geometric sampling of Envisat limits its ability to sample the whole floe

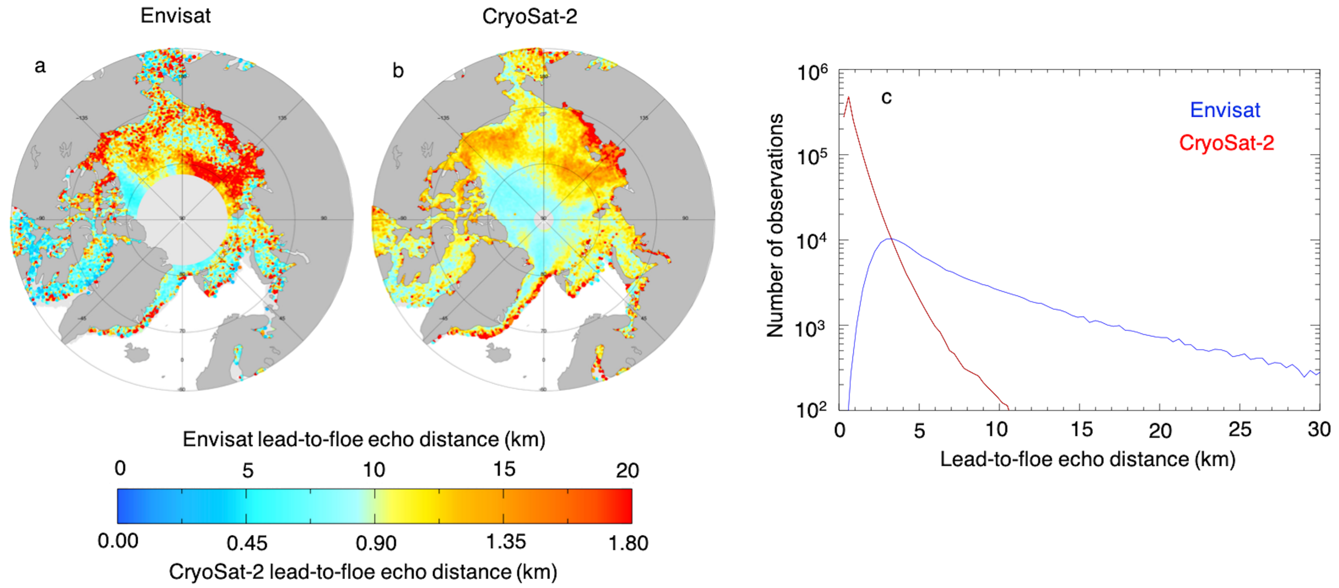

Figure 3. Lead-to-floe echo distances from Envisat and CryoSat-2 for the common mission period. Maps of lead-to-floe echo distance for (a) Envisat and (b) CryoSat-2 are produced on a 5 km^2 Polar Stereographic grid by averaging all measurements within a 25 km radius of the center of each grid cell, with each measurement receiving equal weighting. The maximum ice extent mask for the common mission period is shown in light gray. (c) Number of individual lead-to-floe echo distances over the common mission region of coverage.

size distribution compared with CryoSat-2, as its sampling is limited to longer floes, with sufficient surface area a given distance from a lead.

4. Impact of Lead and Floe Sampling on Sea Ice Thickness

4.1. Sea Ice Thickness Calculation

We calculate sea ice thickness from Envisat and CryoSat-2 using the method developed at the Centre for Polar Observation and Modelling for pulse-limited radar altimeter missions such as ERS-1, ERS-2 [Laxon et al., 2003], and Envisat [Giles et al., 2008; Ridout, 2012] and later adapted for SAR and SAR interferometric mode CryoSat-2 data [Laxon et al., 2013; Tilling et al., 2018]. Following surface type classification (section 3.1), we estimate the elevation of lead and floe surfaces by retracking each waveform to select a consistent point on the leading edge that corresponds to the surface at nadir. Different retrackers are used for Envisat and CryoSat-2 waveforms to limit intermission elevation biases associated with applying noninstrument-specific processing. To retrack Envisat sea ice floe echoes we use an offset center of gravity routine with a 50% threshold [Ridout, 2012]. For CryoSat-2 we apply a Threshold First-Maximum Retracker Algorithm at 70% to sea ice floes [Tilling et al., 2018]. Sea ice floe echoes are ignored if their leading edge width (LEW) exceeds a maximum value. A wide leading edge may be caused by off-nadir reflection from leads [Armitage & Davidson, 2014] or reflection from a very rough surface such as a heavily deformed or ridged ice, which produce anomalously low surface elevations. For Envisat we calculate the LEW as the number of bins between the 50% and 30% offset center of gravity retracking point and remove waveforms with widths greater than four bins [Ridout, 2012]. The CryoSat-2 LEW is the number of bins between the Threshold First-Maximum Retracker Algorithm at 70% and 30% and echoes with a LEW greater than three bins are removed. For both satellites we apply the Giles Gaussian-exponential retracking method to leads [Giles et al., 2007].

Following waveform retracking and filtering, we apply the same processing to Envisat and CryoSat-2 waveforms. Sea ice freeboard is calculated as the difference in elevation between the snow-ice interface and that of the surrounding ocean, with a correction applied to account for the reduced propagation speed of the radar signal through the snow on sea ice. Sea ice freeboard is converted to ice thickness by assuming that the snow-ice interface dominates radar returns and the ice floats in hydrostatic equilibrium and applying values for the densities of ice, snow, and water as well as the snow depth. We do not produce sea ice thickness

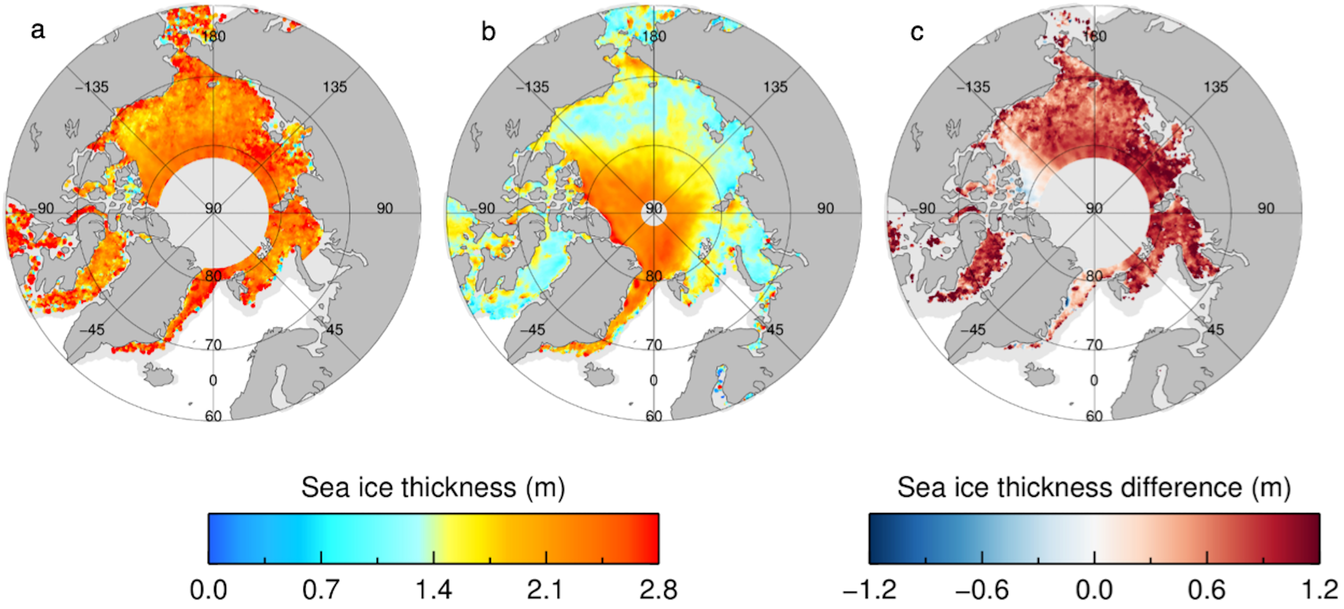

Figure 4. Sea ice thickness from Envisat and CryoSat-2 for the common mission period. (a) Envisat sea ice thickness. (b) CryoSat-2 sea ice thickness. (c) Sea ice thickness difference (Envisat minus CryoSat-2). Monthly sea ice thickness data are output on to a 5 km^2 Polar Stereographic grid by averaging all measurements within a 50 km radius with equal weighting. These are combined for the common mission period by averaging monthly means at each grid location. (a and b) All available data where three or more months are averaged. (c) The difference for grid cells where both Envisat and CryoSat-2 data is present. The maximum ice extent mask for the common mission period is shown in light gray.

estimates during summer as melt ponds make it difficult to discriminate between measurements from leads and the ice surface. We produce Envisat sea ice thickness estimates from October 2005 onwards, due to the availability of ancillary sea ice-type data (section 3.1). A comprehensive description of our sea ice processing and ancillary datasets is given in Tilling et al. [2018].

4.2. Envisat and CryoSat-2 Sea Ice Thickness

There are visible differences in maps of sea ice thickness from Envisat (Figure 4a) and CryoSat-2 (Figure 4b) during their common mission period. Unlike CryoSat-2, Envisat does not resolve the clear transition from thicker MYI north of the Canadian Archipelago to the surrounding thinner seasonal ice cover. The resulting sea ice thickness differences (Envisat minus CryoSat-2; Figure 4c) show that Envisat thicknesses are consistently higher than those from CryoSat-2, by an average of 68 cm over their common mission period and ROC. Envisat overestimates sea ice thickness compared with CryoSat-2 by an average of 80 cm over FYI and 23 cm over MYI. In the remainder of section 4 we consider the influence of geometric sampling on the observed intermission sea ice thickness differences.

4.3. Undersampling of the Sea Ice Thickness Distribution with Envisat

By preferentially sampling longer sea ice floes (sections 3.2 and 3.3), Envisat will be biased towards thicker ice. To investigate the impact of floe length sampling on sea ice thickness estimates we compute the mean thickness along each satellite-observed floe length sequence for Envisat and CryoSat-2. Using all available data over each mission timeframe, we find that both satellites measure an increase in average sea ice thickness over the sea ice growth season (October to April; Figure 5a). However, for each individual month there is an increase in sea ice thickness with satellite-observed floe length from CryoSat-2 that is not present for Envisat. We find similar over the common mission period and ROC, where Envisat floe thickness is independent of satellite-observed floe length (Figure 5b). We conclude that the short satellite-observed floe lengths from Envisat are from short sections of the longer, thicker floes observed by CryoSat-2. As a consequence, Envisat does not resolve the lower end of the sea ice thickness probability density function (PDF; Figure 5c). The sea ice thickness PDF is measured more extensively with CryoSat-2, which follows that of Envisat at ice thicknesses of 3.2 m and above. The inability of Envisat to sample shorter, thinner sea ice floes will contribute to its overestimation of ice thickness relative to CryoSat-2 (section 4.2 and Figure 4).

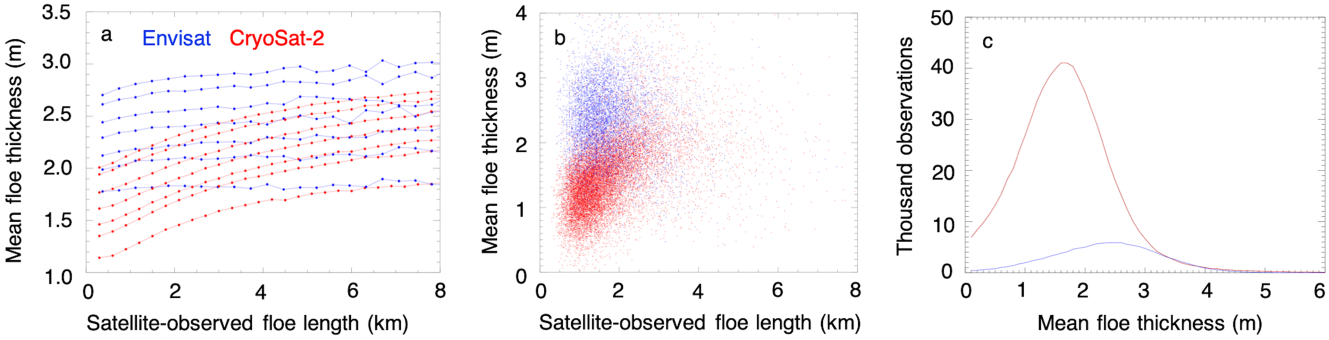

Figure 5. The relationship between sea ice thickness and satellite-observed floe length measured by Envisat (blue) and CryoSat-2 (red). (a) Monthly mean sea ice thickness and satellite-observed floe length for individual floes for all available data from each satellite. Lines from bottom to top are progressive for each month from October to April. (b) Monthly mean sea ice thickness and floe length averaged on a 0.4° latitude by 4.0° longitude grid, over the common mission period and region of coverage. (c) The number of sea ice floes with a given mean floe thickness in 10-cm bins, for individual floes over the common mission period and region of coverage.

4.4. Correcting the Envisat Sea Ice Thickness Bias

To reconcile sea ice thickness estimates from Envisat and CryoSat-2, we must correct for the Envisat thickness bias that is introduced by its geometric sampling limitations. Here we consider the relationship between the bias and Envisat lead-to-floe echo distance (section 3.3). We use lead-to-floe echo distance, rather than satellite-observed floe length (section 3.2), because the former is a measurable parameter that represents the inability of Envisat to resolve discrete surfaces. We calculate the Envisat sea ice thickness bias by averaging individual Envisat and CryoSat-2 thicknesses on to a common 0.5° latitude by 2.0° longitude grid for each month and subtracting CryoSat-2 from Envisat. Thicknesses outside the range −3 to +8 m are removed before gridding. Negative ice thickness values are permitted to ensure average thickness is not biased high [Tilling et al., 2018]. We remove Envisat grid cells where fewer than three thickness measurements were averaged or the standard error exceeds 50 cm. CryoSat-2 grid cells are removed if fewer than five thickness measurements were averaged or the standard error exceeds 40 cm. We smooth Envisat lead-to-floe echo distances along track with an averaging window of 200 km centered at each sampling location, then average monthly values onto the same 0.5° latitude by 2.0° longitude grid as the sea ice thickness bias. Lead-to-floe echo distances of greater than 50 km are removed before averaging, and grid cells are considered unreliable if they have fewer than 10 lead-to-floe echo distance values or a standard error exceeding 1 km. Values for the Envisat sea ice thickness bias over the common mission period are then averaged in 1 km bins of lead-to-floe echo distance for FYI and MYI separately (Figure 6).

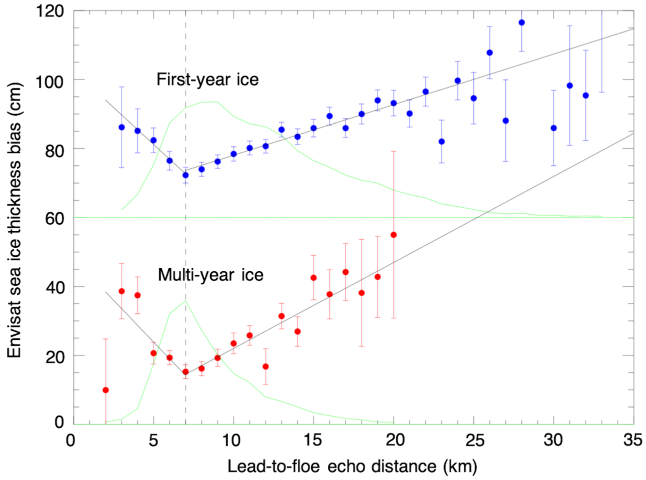

Figure 6. Envisat sea ice thickness bias correction for first-year ice (blue) and multiyear ice (red). The Envisat sea ice thickness bias (Envisat minus CryoSat-2) is shown as a function of lead-to-floe echo distance, where error bars are the standard error on thickness within 1 km lead-to-floe distance bins. The functional fit (sold black lines) is applied to Envisat point measurements of sea ice thickness, depending on their ice type and grid cell. Also shown is the normalized occurrence of gridded lead-to-floe echo distances (solid green lines) and the 7 km lead-to-floe distance separating the two linear regressions (dashed black lines).

For each sea ice type, we compute a correction function for the Envisat ice thickness bias (Figure 6). We fit two linear regressions to the bin-averaged bias data, weighted by the standard error. The first fit is to lead-to-floe echo distances increasing from 7 km to the cutoff point of the bias PDFs. The second is from the start of the bias PDFs increasing to 6 km lead-to-floe echo distances, extending to 7 km. Above lead-to-floe echo distances of 7 km, every additional kilometer between a lead and floe measurement introduces an Envisat sea ice thickness bias of 1.5 cm over FYI and 2.5 cm over MYI. The Envisat ice thickness bias increases with increasing lead-to-floe echo distance above 7 km, as Envisat fails to resolve a progressively greater fraction of the ice thickness distribution. Below apparent lead-to-floe echo distances of 7 km, an ice thickness bias of 4.8 cm is introduced over MYI and 4.2 cm for FYI for each kilometer reduction in lead-to-floe echo distance. This is a consequence of waveform snagging to off-nadir leads, which increases the Envisat

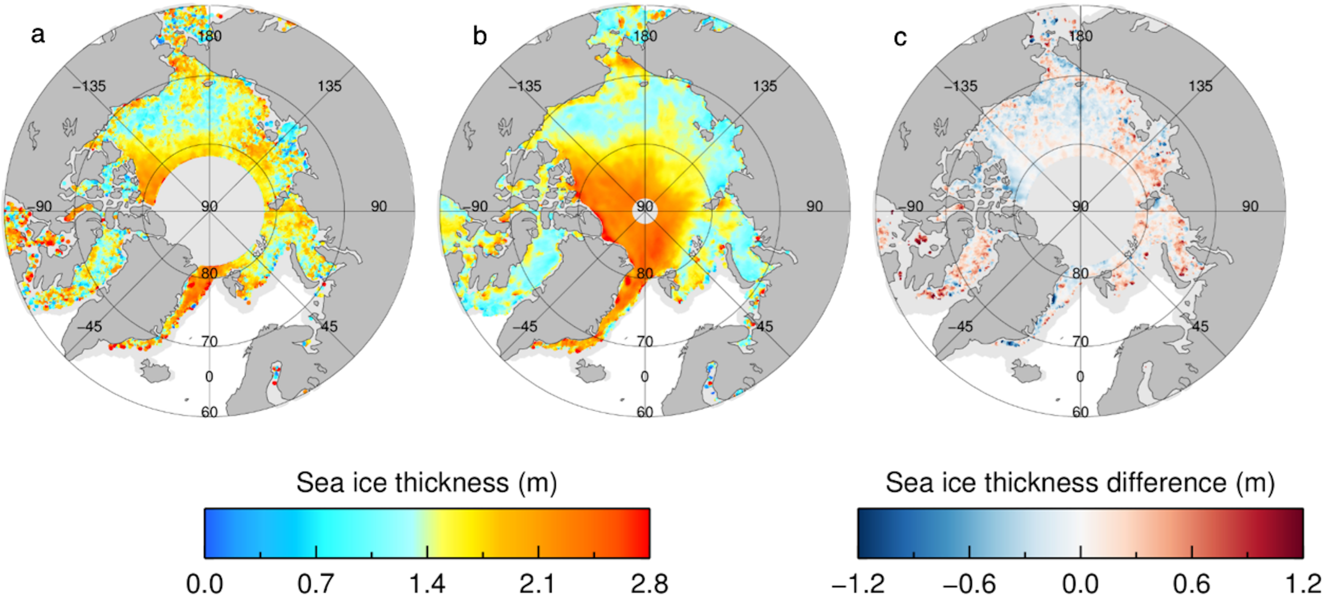

Figure 7. Sea ice thickness from bias-corrected Envisat and CryoSat-2 for the common mission period. (a) Bias-corrected Envisat sea ice thickness. (b) CryoSat-2 sea ice thickness, which is replicated from Figure 4b. (c) Sea ice thickness difference (bias-corrected Envisat minus CryoSat-2). Monthly sea ice thickness data are output on to a 5 km^2 Polar Stereographic grid by averaging all measurements within a 50 km radius with equal weighting. These are combined for the common mission period by averaging monthly means at each grid location. (a and b) All available data where three or more months are averaged. (c) The difference for grid cells where both Envisat and CryoSat-2 data is present. The maximum ice extent mask for the common mission period is shown in light gray.

range to the sea surface [Armitage & Davidson, 2014] and effectively thickens sea ice floes. This thickening increases the Envisat sea ice thickness bias and causes the negative gradient of the fit, from which we estimate the effective footprint of Envisat over sea ice to be 7 km, before all floe returns are contaminated by off-nadir reflection from leads. For each month and ice type, we create our Envisat sea ice thickness bias correction by multiplying gridded lead-to-floe echo distances by the correction function. Envisat sea ice thickness estimates are reconciled with those from CryoSat-2 by correcting point estimates of thickness depending on their ice type and lead-to-floe echo distance of their grid cell. Where the lead-to-floe echo distance is outside the range 2.0 to 35.0 km or has been flagged as unreliable, the correction is not applied and the ice thickness is removed from processing.

5. Sea Ice Thickness Corrected for Lead and Floe Sampling

5.1. Corrected Envisat and CryoSat-2 Sea Ice Thickness

After applying our sea ice thickness bias correction to Envisat data (section 4.4), there are clear similarities in maps of ice thickness from Envisat (Figure 7a) and CryoSat-2 (Figure 7b) combined for their common mission period. The typical spatial distribution of sea ice thickness associated with MYI and FYI cover is now visible in Envisat data. Sea ice thickness differences are also reduced (Figure 7c), with an average ice thickness difference of only −1 cm over the common mission period and ROC, with an average difference of −2 and 1 cm for FYI and MYI, respectively—values that are negligible by comparison to typical sea ice thickness uncertainties [Tilling et al., 2018]. Sea ice thickness differences between Envisat and CryoSat-2 still exist, particularly where insufficient Envisat data are averaged to eliminate the random noise introduced by the speckle on radar waveforms, such as in Hudson Bay and the Bering and Kara Seas. Despite these remaining differences, we have shown that by applying a physically based ice thickness correction to Envisat data to account for its geometric sampling limitations, we are able to significantly reduce the average thickness difference between Envisat and CryoSat-2 over both FYI and MYI.

5.2. Estimation of Sea Ice Thickness Uncertainty

We estimate the uncertainty on monthly estimates of bias-corrected Envisat and CryoSat-2 sea ice thickness by considering the contributions due to uncertainties in individual freeboard retrievals and uncertainties in

Table 1
The Bias-Corrected Envisat Sea Ice Thickness Error Budget, by Ice Type, for Autumn (October) and Spring (April)

	Autumn (October)		Spring (April)	
	FYI Mean thickness: 1.0 m	MYI Mean thickness: 1.5 m	FYI Mean thickness: 1.8 m	MYI Mean thickness: 2.6 m
Floe height	15.4	2.6	8.6	2.9
Sea surface height	28.4	7.7	13.7	5.1
Snow depth	16.6	16.9	15.1	16.4
Snow density	11.1	11.3	9.2	10.0
Sea ice density	7.1	5.4	7.1	5.4
Total error	40.7	23.0	26.0	21.0

Note. The error budget is the monthly average from October 2005 to April. Columns show the percentage contribution of each parameter to the total estimated ice thickness error. These contributions are combined in a root-sum-square manner to give an estimate of the total monthly sea ice thickness error. FYI = first-year ice; MYI = multiyear ice.

the parameters required to convert freeboard to thickness: snow depth, snow density, and sea ice density. We assume that the contribution of uncertainty in seawater density is negligible [Giles et al., 2007; Kurtz et al., 2013]. Individual sea ice thickness estimates are output on to a 5 km^2 Polar Stereographic grid for each month by averaging all thickness measurements within a 50 km radius, with all points receiving equal weighting. Monthly averaging provides regular, complete data coverage across the ROC of both satellites considering the 35-day repeat cycle of the Envisat orbit and 30-day subcycle of CryoSat-2. It also reduces the sea ice thickness uncertainty introduced by speckle on individual radar altimeter echoes and the associated noise in maps of sea ice thickness [Laxon et al., 2013; Wingham et al., 2006].

We calculate the error budgets for Envisat and CryoSat-2 using all available data over each mission timeframe. Within our 50 km averaging radius, individual sea ice freeboard measurements have a standard deviation averaging about 10 and 12 cm from Envisat and CryoSat-2, respectively. The standard deviation of freeboard is a consequence of real variations in freeboard, and speckle noise on floe heights, and uncertainties in the sea surface height (SSH). Floe height variations due to speckle decorrelate from one measurement to the next, whereas SSH is estimated by averaging individual lead elevations along 200 km of a satellite orbit, so will remain correlated within the averaging radius [Tilling et al., 2018]. For each grid cell we estimate the uncertainty in SSH, σ_{SSH}, by calculating the difference in SSH at satellite crossover points within our 50 km averaging radius, computing the standard deviation of the difference, then reducing by a factor of $\sqrt{2}$ to get uncertainty on a single SSH measurement. Crossovers are limited to cases where the time difference between ascending and descending orbits is 1 day or less, over which there should be little change in true SSH. This results in an average σ_{SSH} of 7.9 and 5.6 cm across the full Envisat and CryoSat-2 ROC, respectively. Crossover differences will include contributions from errors in geophysical corrections that are not important for freeboard estimates [Ricker et al., 2016], and so our σ_{SSH} values are likely to be an overestimate. However, both σ_{SSH} and its contribution to the sea ice thickness error budget (Table 1) are highly dependent on season and ice type, suggesting a dominant contribution from the irregular sampling of leads that results in an error where the SSH is interpolated at each floe location. The quality of the interpolated SSH will depend on the number of available lead measurements, which is lower for Envisat than CryoSat-2 (Figure 1). To calculate the uncertainty in floe height for each grid cell we take all contributing orbits in turn and compute the standard deviation of along-track floe height within our 50 km averaging radius. The final uncertainty in floe height, σ_{height}, is the mean of these individual standard deviations, weighted by the number of floe heights along the orbit segment. For a given grid cell σ_{SSH} and σ_{height} are combined to give the uncertainty in sea ice freeboard, σ_{f_c}, using

$$\sigma_{f_c} = \sqrt{\frac{(\sigma_{SSH})2}{N_o} + \frac{(\sigma_{height})2}{N_m}}, \tag{1}$$

where N_o is the number of contributing orbits and N_m is the number of individual freeboards within each grid cell. The contribution of sea ice freeboard uncertainty to sea ice thickness uncertainty, ε_{f_c}, is then given by

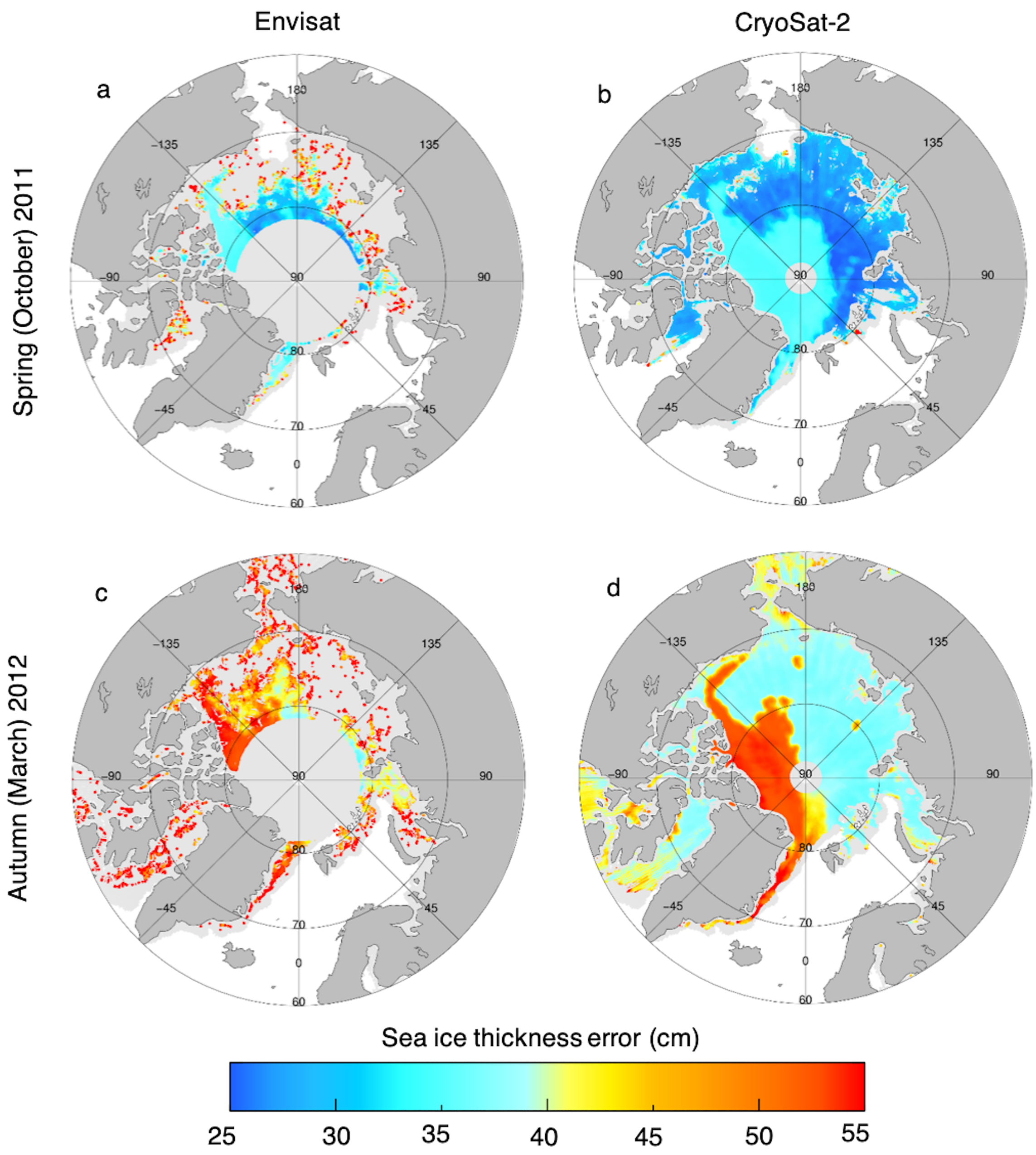

Figure 8. Error budget for bias-corrected Envisat and CryoSat-2 sea ice thickness for the 2011–2012 ice growth season. (a and b) Sea ice thickness error for autumn (October) 2011 for Envisat and CryoSat-2, respectively. (c and d) Sea ice thickness error for spring (March) 2012 for Envisat and CryoSat-2, respectively. Errors are calculated on our monthly sea ice thickness data, which are output on to a 5 km^2 Polar Stereographic grid by averaging all measurements within a 50 km radius with equal weighting, to reduce speckle uncertainty. The ice extent mask for each month is shown in light gray.

$$\varepsilon_{f_c} = \left(\frac{\rho_w}{\rho_w - \rho_i}\right)\sigma_{f_c}, \tag{2}$$

where ρ_w and ρ_i are the densities of seawater and sea ice respectively [Tilling et al., 2018]. Uncertainties in snow depth, snow density, and sea ice density and their contribution to ice thickness uncertainty are calculated in the same way as Tilling et al. [2018]. To estimate the sea ice thickness error resulting from our Envisat thickness bias correction we computed the mean squared difference between our derived bias-correction function and the observed biases across the lead-to-floe echo distance PDF (Figure 6). The resulting error in the mean bias was negligible compared with those from the other parameters. Finally,

Table 2

The CryoSat-2 Sea Ice Thickness Error Budget, by Ice Type, for Autumn (October) and Spring (April)

	Autumn (October)		Spring (April)	
	FYIMean thickness: 0.8 m	MYIMean thickness: 1.7 m	FYIMean thickness: 1.8 m	MYIMean thickness: 3.0 m
Floe height	12.1	1.0	3.0	0.8
Sea surface height	22.7	3.9	7.6	2.4
Snow depth	21.1	14.7	15.5	14.2
Snow density	14.1	9.8	9.5	8.6
Sea ice density	7.1	5.4	7.1	5.4
Total error	38.2	19.1	21.4	17.7

Note. The error budget is the monthly average over October 2010–April 2018. Columns show the percentage contribution of each parameter to the total estimated ice thickness error. These contributions are combined in a root-sum-square manner to give an estimate of the total monthly sea ice thickness error. FYI = first-year ice; MYI = multiyear ice.

we sum the uncertainties of each contributing factor in a root-sum-square manner to estimate the total uncertainty on individual gridded thicknesses.

The total error on our bias-corrected Envisat and CryoSat-2 sea ice thickness estimates increases with increasing ice thickness over the growth season (Figure 8). Snow depth is a major contributor to this growth in sea ice thickness error, as snow accumulates and the associated standard deviation of depth anomaly increases. However, the values we use for climatology snow depth and density uncertainties are likely to be an overestimate according to the data authors [Warren et al., 1999]. Sea ice thickness errors over MYI are greater than over FYI, as we half the FYI climatology snow depth and uncertainty values [Tilling et al., 2018]. We investigate the relative contribution of each factor to the monthly sea ice thickness error for all available data from each satellite. The error contributions for autumn (October) and spring (March) are different for Envisat (Table 1) and CryoSat-2 (Table 2). For both satellites, the total percentage error of FYI exceeds that of MYI throughout the growth season, due to the greater contribution of floe height and SSH uncertainty. Fewer orbits on average are present within a 50 km radius over FYI as the orbit ground track spacing increases at lower latitudes. Over FYI in October, SSH uncertainty is the dominant contributing factor in our sea ice thickness error budget for Envisat and CryoSat-2. Its influence decreases over the growth season, associated with an increase in the number of available SSH measurements, and snow depth uncertainties become dominant. Over MYI, snow depth is the dominant contributing factor to the ice thickness error throughout the growth season for both Envisat and CryoSat-2.

5.3. Evaluation

Few independent sea ice thickness data were acquired over the common mission period of Envisat and CryoSat-2, and so we evaluate our bias-corrected Envisat sea ice thicknesses using data from the whole of the Envisat mission. We compare our Envisat sea ice thickness estimates to independent estimates of sea ice thickness and draft acquired from airborne and ocean-based platforms. The evaluation uses estimates of sea ice thicknesses derived from NASA Operation IceBridge (OIB) airborne radar and laser altimeter measurements [Kurtz et al., 2013], sea ice plus snow thickness derived by from ESA CryoSat-2 Validation Experiment (CryoVEx) airborne laser altimeter and electromagnetic sounding measurements [Haas et al., 2009], estimates of sea ice draft derived from moored-buoy upward looking sonar measurements as part of the Beaufort Gyre Exploration Program (BGEP) based at the Woods Hole Oceanographic Institution (http://www.whoi.edu/beaufortgyre), and estimates of sea ice draft derived from Sea Ice Experiments (SCICEX) submarine upward looking sonar measurements [NSIDC, 1998, updated 2006]. The CryoVEx sea ice plus snow thicknesses, BGEP ice drafts and SCICEX ice drafts are converted to ice thickness using the adapted snow climatology that is applied in our sea ice processing [Tilling et al., 2018; Warren et al., 1999]. Final OIB L4 IDCSI4 data are used from 2009–2012, CryoVEx data from 2011–2012, BGEP data from 2005–2012, and SCICEX from 2005. Both the OIB and CryoVEx measurements were only collected during spring (March and April), but they survey a variety of sea ice thickness and type [Tilling et al., 2018]. The BGEP observations are available at four fixed locations year-round in the Beaufort Sea, and the SCICEX submarine traverse of the Beaufort occurred in November 2005.

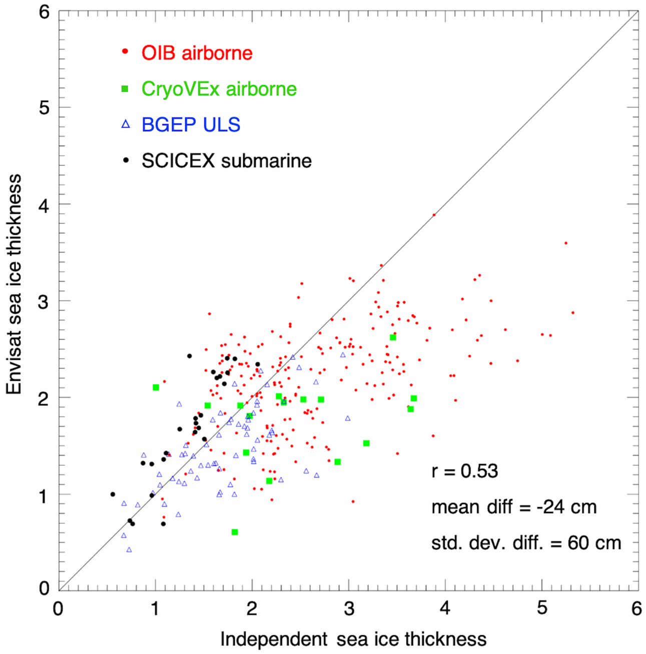

Figure 9. Evaluation of bias-corrected Envisat sea ice thickness. Envisat sea ice thicknesses are compared with airborne data from the NASA Operation IceBridge (OIB) campaign from March to April 2009–2012 (red dots) and the ESA CryoVEx campaign from March to April 2011–2012 (green squares), Beaufort Gyre Exploration Program (BGEP) upward looking sonar (ULS) measurements from October to April 2005–2012 (blue triangles), and Sea Ice Experiments (SCICEX) submarine measurements from November 2005 (black dots).

To compare our Envisat estimates to the OIB and CryoVEx data, we averaged all datasets onto a 0.4° latitude by 4° longitude grid, which resulted in 224 distinct OIB values and 16 CryoVEx values. For the BGEP comparison we took monthly averages of all Envisat sea ice thickness estimates within 100 km of each mooring and compared with monthly average ice thickness from each mooring, resulting in 65 distinct values. To compare to SCICEX submarine data we averaged all Envisat sea ice thickness estimates for November 2005 within a 50 km radius of the midpoint of each track and compared to the average submarine ice thickness for the track, leaving 25 distinct values. Overall, the average difference between our Envisat sea ice thickness estimates and those from independent measurements is 24 cm with a standard deviation of 60 cm (Figure 9). For comparison, the mean difference and standard deviation of our CryoSat-2 sea ice thickness estimates with 1,232 gridded in situ observations are 2 mm and 34 cm, respectively [Tilling et al., 2018]. The majority of the spread in our Envisat evaluation is caused by Envisat underestimating sea ice thickness compared with OIB over thick ice. The independent estimates of sea ice thickness are still derived products, like Envisat, and the absolute differences between thickness estimates from satellite and other observations can arise through uncertainties in either dataset. However, the independent datasets provide improved spatial resolution in the absence of in situ measurements of sea ice thickness with suitable spatial and temporal coverage.

6. Conclusions

We have shown that Envisat and CryoSat-2 do not sample the same distribution of leads and floes in Arctic sea ice covered regions. Envisat experiences more measurement dropout than CryoSat-2 as its larger footprint frequently covers a mixture of surface types. As a consequence, Envisat preferentially samples wider, thicker sea ice floes and is more sensitive to effective thickening caused by off-nadir ranging to leads. These contribute to a positive ice thickness bias from Envisat when compared with CryoSat-2 over their common mission period and ROC. On this basis, we have developed a physically based Envisat sea ice thickness bias correction by considering the relationship between the thickness bias and the along-track distance between an Envisat lead measurement and the closest detected floe. Applying the bias correction reduces the average thickness difference between the satellite missions from 68 to −1 cm. In future, a similar Arctic-wide comparison could be performed with satellite data from CryoSat-2 and the NASA ICESat-2 laser altimeter, which has the potential to further improve resolution over sea ice regions. We will also work to develop a reconciled sea ice thickness time series from Envisat and CryoSat-2 is. This is complicated by the dropout of Envisat measurements over regions with high lead densities and smaller sea ice floes that are typically associated with younger, thinner ice. The dropout will bias the average Envisat sea ice thickness high compared with CryoSat-2 if all the available data from both missions are included, and so it must be accounted for to produce a continuous sea ice thickness time series from the start of the Envisat mission in 2002.

Acknowledgments
This work was funded by the UK Natural Environment Research Council Centre for Polar Observation and Modelling and the European Space Agency. The Envisat and CryoSat-2 sea ice thickness products are available on the CPOM data portal at http://www.cpom.ucl.ac.uk/csopr/seaice.html. We wish to thank those who provided the ancillary data required to deliver our sea ice thickness product: ESA, for the Envisat Level 2 and CryoSat-2 Level 1b data; NASA Goddard for their sea ice concentration and Operation Icebridge data; OSI SAF for their sea ice-type data; the CryoVEx EM-bird team, Woods Hole for their BGEP ULS data; the SCICEX team for their submarine ULS data; and NSIDC for data hosting.

References

Andersen, S., Breivik, L.-A., Eastwood, S., Godøy, Ø., Lavergne, T., Lind, M., et al. (2012). *Ocean and Sea Ice SAF, Sea Ice Product Manual, version 3.8, OSI SAF document no. SAF/OSI/met.no/TEC/MA/125*, (p. 37). Darmstadt, Germany: EUMETSAT.

Armitage, T. W. K., & Davidson, M. (2014). Using the interferometric capabilities of the ESA CryoSat-2 mission to improve the accuracy of sea ice freeboard retrievals. *IEEE Transactions on Geoscience and Remote Sensing*, *52*(1), 529–536.

Cavalieri, D. J., Parkinson, C. L., Gloersen, P., & Zwally, H. J. (1996, updated yearly). Sea ice concentrations from Nimbus-7 SMMR and DMSP SSM/I-SSMIS passive microwave data [concentration], edited, NASA DAAC at the National Snow and Ice Data Center, Boulder, Colorado, USA.

Chelton, D. B., Ries, J. C., Haines, B. J., Fu, L.-L., & Callahan, P. S. (2001). Satellite altimetry. In L.-L. Fu, & A. Cazenave (Eds.), *Satellite altimetry and earth sciences*, (pp. 1–131). London, UK and San Diego, USA: Academic Press.

Connor, L. N., Laxon, S. W., Ridout, A. L., Krabill, W. B., & McAdoo, D. C. (2009). Comparison of Envisat radar and airborne laser altimeter measurements over Arctic sea ice. *Remote Sensing of Environment*, *113*(3), 563–570.

Drinkwater, M. R. (1991). Ku band airborne radar altimeter observations of marginal sea ice during the 1984 marginal ice-zone experiment. *Journal of Geophysical Research*, *96*, 4555–4572. https://doi.org/10.1029/90JC01954

ESA (2007). *Envisat RA2-MWR Product Handbook, Issue 2.2*, (p. 204). Frascati, Italy: ESA.

ESA/MSSL (2013). *CryoSat Product Handbook*, (p. 103). Italy and Surrey, UK: ESRIN, ESA and Mullard Space Science Laboratory/University College London Frascati.

Giles, K. A., Laxon, S. W., & Ridout, A. L. (2008). Circumpolar thinning of Arctic sea ice following the 2007 record ice extent minimum. *Geophysical Research Letters*, *35*, L22502. https://doi.org/10.1029/2008gl035710

Giles, K. A., Laxon, S. W., Wingham, D. J., Wallis, D. W., Krabill, W. B., Leuschen, C. J., et al. (2007). Combined airborne laser and radar altimeter measurements over the Fram Strait in May 2002. *Remote Sensing of Environment*, *111*(2–3), 182–194.

Guerreiro, K., Fleury, S., Zakharova, E., Kouraev, A., Rémy, F., & Maisongrande, P. (2017). Comparison of CryoSat-2 and ENVISAT radar freeboard over Arctic sea ice: Toward an improved Envisat freeboard retrieval. *The Cryosphere*, *11*(5), 2059–2073.

Haas, C., Lobach, J., Hendricks, S., Rabenstein, L., & Pfaffling, A. (2009). Helicopter-borne measurements of sea ice thickness, using a small and lightweight, digital EM system. *Journal of Applied Geophysics*, *67*(3), 234–241.

Kurtz, N. T., Farrell, S. L., Studinger, M., Galin, N., Harbeck, J. P., Lindsay, R., et al. (2013). Sea ice thickness, freeboard, and snow depth products from Operation IceBridge airborne data. *The Cryosphere*, *7*(4), 1035–1056.

Kwok, R., & Cunningham, G. F. (2015). Variability of Arctic sea ice thickness and volume from CryoSat-2. *Philosophical Transactions of the Royal Society A - Mathematical Physical and Engineering Sciences*, *373*(2045), 20140157. https://doi.org/10.1098/rsta.2014.0157

Laxon, S. (1994). Sea ice extent mapping using the ERS-1 radar altimeter. *EARSeL Advances in Remote Sensing*, *3*, 112–116.

Laxon, S., Peacock, N., & Smith, D. (2003). High interannual variability of sea ice thickness in the Arctic region. *Nature*, *425*(6961), 947–950. https://doi.org/10.1038/nature02050

Laxon, S., Laxon, S. W., Giles, K. A., Ridout, A. L., Wingham, D. J., Willatt, R., et al. (2013). CryoSat-2 estimates of Arctic sea ice thickness and volume. *Geophysical Research Letters*, *40*, 732–737. https://doi.org/10.1002/grl.50193

NSIDC (1998, updated 2006). *Submarine upward looking sonar ice draft profile data and statistics*, Version 1, edited. Boulder, Colorado, USA: National Snow and Ice Data Center.

Paul, S., Hendricks, S., Ricker, R., Kern, S., & Rinne, E. (2018). Empirical parametrization of Envisat freeboard retrieval of Arctic and Antarctic sea ice based on CryoSat-2: Progress in the ESA Climate Change Initiative. *The Cryosphere*, *12*(7), 2437–2460. https://doi.org/10.5194/tc-12-2437-2018

Peacock, N. R., & Laxon, S. W. (2004). Sea surface height determination in the Arctic Ocean from ERS altimetry. *Journal of Geophysical Research*, *109*, C07001. https://doi.org/10.1029/2001JC001026

Ricker, R., Girard-Ardhuin, F., Krumpen, T., & Lique, C. (2018). Satellite-derived sea ice export and its impact on Arctic ice mass balance. *The Cryosphere*, *12*(9), 3017–3032. https://doi.org/10.5194/tc-12-3017-2018

Ricker, R., Hendricks, S., & Beckers, J. F. (2016). The impact of geophysical corrections on sea-ice freeboard retrieved from satellite altimetry. *Remote Sensing*, *8*(4), 317. https://doi.org/10.3390/rs8040317

Ridout, A. (2012). *Sea ice climate change initiative: Phase 1—Algorithm Theoretical Basis Document (ATBDv0), ESA document no. SICCI-ATBDv0-07-12*, (p. 23). Italy and Surrey, UK: ESRIN, ESA and Mullard Space Science Laboratory/University College London Frascati.

Schwegmann, S., Rinne, E., Ricker, R., Hendricks, S., & Helm, V. (2016). About the consistency between Envisat and CryoSat-2 radar freeboard retrieval over Antarctic sea ice. *The Cryosphere*, *10*(4), 1415–1425. https://doi.org/10.5194/tc-10-1415-2016

Tilling, R. L., Ridout, A., & Shepherd, A. (2018). Estimating Arctic sea ice thickness and volume using CryoSat-2 radar altimeter data. *Advances in Space Research*, *62*(6), 1203–1225. https://doi.org/10.1016/j.asr.2017.10.051

Tilling, R. L., Ridout, A., Shepherd, A., & Wingham, D. J. (2015). Increased Arctic sea ice volume after anomalously low melting in 2013. *Nature Geoscience*, *8*(8), 643–646. https://doi.org/10.1038/ngeo2489

Warren, S. G., Rigor, I. G., Untersteiner, N., Radionov, V. F., Bryazgin, N. N., Aleksandrov, Y. I., & Colony, R. (1999). Snow depth on Arctic sea ice. *Journal of Climate*, *12*(6), 1814–1829. https://doi.org/10.1175/1520-0442(1999)012<1814:SDOASI>2.0.CO;2

Wingham, D. J., Francis, C. R., Baker, S., Bouzinac, C., Brockley, D., Cullen, R., et al. (2006). CryoSat: A mission to determine the fluctuations in Earth's land and marine ice fields. *Advances in Space Research*, *37*(4), 841–871. https://doi.org/10.1016/j.asr.2005.07.027